energies

MDPI

Article

Modelling and Optimization of a Small Diesel Burner for Mobile Applications

Zahra S. Musavi [1,*], Henrik Kusar [1], Robert Andersson [2] and Klas Engvall [1]

[1] Department of Chemical Engineering, KTH Royal Institute of Technology, Teknikringen 42, 11428 Stockholm, Sweden; hkusar@kth.se (H.K.); kengvall@kth.se (K.E.)
[2] Reformtech Heating Technologies AB, Skalholtsgatan 9, 164 40 Kista, Sweden; robert.andersson@reformtech.se
* Correspondence: musavi@kth.se; Tel.: +46-8790-6602

Received: 11 September 2018; Accepted: 21 October 2018; Published: 25 October 2018

Abstract: While extensive research has been done on improving diesel engines, much less has been done on auxiliary heaters, which have their own design challenges. The study analyzes how to optimize the combustion performance of an auxiliary heater, a 6 kW diesel burner, by investigating key parameters affecting diesel combustion and their properties. A model of a small diesel heater, including a simulation of fuel injection and combustion process, was developed step-wise and verified against experimental results that can be used for scaling up to 25 kW heaters. The model was successfully applied to the burner, predicting the burner performance in comparison with experimental results. Three main variables were identified as important for the design. First, it was concluded that the distance from the ring cone to the nozzle is essential for the fluid dynamics and flame location, and that the ring cone should be moved closer to the nozzle for optimal performance. Second, the design of the swirl co-flow is important, and the swirl number of the inlet air should be kept above 0.6 to stabilize the flame location for the present burner design. Finally, the importance of the nozzle diameter to avoid divergent particle vaporization was pointed out.

Keywords: diesel combustion; CFD modelling; nozzle diameter; NOx emission; swirl number; design optimization

1. Introduction

The transportation sector accounted for nearly 29 and 26% of the greenhouse gas emissions in United States (2016) and European Union (EU) (2015), respectively, primarily involving combustion of fossil fuels (over 90%) for road, rail, air, and marine transportation [1–3]. In spite of efforts replacing the combustion engine with alternative technologies, such as electric propulsion systems, combustion will remain the prevailing method for energy utilization in the transportation sector, especially for heavy duties [4]. Therefore, there is a need to invest in optimizing the design of combustion equipment for increased efficiency, which is also driven by requirements for minimizing emissions of pollutants [5].

Modern diesel engines generally do not generate enough waste heat to be able to heat up the car interior to comfortable temperatures in cold climates (or heats it up very slowly) [6]; therefore, auxiliary diesel heaters are often installed in cold climate regions like northern Europe. Additionally, by preheating the engine with a diesel heater, the start-up emissions from the engine and wear can be drastically reduced as the engine is already at the right operation temperature. Start-up emissions are a big pollution source. Furthermore, heavy duty trucks generally operate in idling mode for 20–40% of their operating times to support comfort systems such as cabin heating, microwave ovens, air condition, and so on. Idling, a very inefficient way to produce the heat and electricity, has been increasing significantly in recent years, partly as a result of the utilization of just in time production

methods [7]. In the case of cabin heating, the use of a diesel heater would efficiently provide the required heat, reducing fuel consumption. These heaters can operate independently of the vehicle engine and could thus also be a good solution for future generation electric cars, because using electricity to generate heat reduces over 30% mileage according to the U.S. Environmental Protection Agency (EPA) and the U.S. Energy Department [8].

Fuel needs to be completely combusted with very low levels of unburnt hydrocarbons, carbon monoxide (CO), and soot left in the exhaust gas, in accordance with legislations [9,10]. The combustion process has a fundamental role in the formation of pollutants. Emissions, especially nitrogen oxides (NOx), which are normally formed at the high-temperature zones of burners, must be avoided during combustion. The impact of these emissions on the environment is reported in the industry and literature [11]. Depending on different engine capacities and automotive types, the power of the heaters typically ranges from 2 to 32 kW [12,13], generally much lower than the power of vehicle engines, with a range of 60–400 kW [14,15]. Although the fuel consumption of a heater is a small portion of a vehicle's total fuel consumption, the combustion characteristics and related emission parameters must be properly designed for a successful and clean performance. The CO emission limit for engines exhausts, according to the Euro 6 legislation, is 500 mg/km. The car emissions are tested with air conditioning and auxiliary heaters turned off, according to WLTP (Worldwide Harmonized Light Vehicle Test Procedure) [16]. The emission criteria for the heating systems are addressed in the Economic Commission for Europe regulation number ECE 122 [17], for instance, stating the limit of 1000 ppm for CO emission. In the future, the heater emissions may also be included in the car total emissions. The future legislation most probably means the rules for heaters will be stricter, so that the acceptable emission levels will be lower. Additionally, the burner design is further complicated by the use of various qualities of fossil diesels and renewable fuels around the world. A profound understanding of the liquid fuel combustion, including atomization and evaporation of fuel, fuel injection system, flow control, interaction between the combustion, swirl, turbulence, and so on [11], is of importance in burner design and operation using different fuels.

A controlled mixing of the oxidant and fuel streams is crucial for an optimized combustion. This is of particular importance in the case of a small burner where the flame center, and thus the high temperatures, should not touch walls and burner components because of the thermal properties of the materials. A commonly used technique to stabilize the flame shape and to limit its length is to surround the fuel spray with a swirling co-flow [18,19]. This creates a recirculation zone confining the spray of droplets, preventing the flame from reaching the opposite wall. A drawback is a possible reduction in temperature at the wall with possible formation of polyaromatic hydrocarbons (PAH) and, subsequently, formation of soot under rich or lean conditions [20]. The degree of swirl is characterized by the swirl number (SN) defined as the ratio of axial flux of tangential momentum to the axial flux of axial momentum [18,21]. The swirling co-flow is controlled by velocity components of the inlet air shaped by the air diffuser configuration and defined by the vane angle, vane, and hub diameters [22].

Besides the air diffuser configuration, other geometrical components such as the gas channel design and cones are also important for forcing the fluids to mix. The effects of the channel walls were investigated by Chong and Hochgreb [23], demonstrating that the presence of burner walls results in formation of a corner recirculation zone. The walls also affect the velocity fields with higher axial velocities for confined flow and an increased reverse flow magnitude. An experimental study by González-Espinosa et al. [24] illustrated the effect of a cone arrangement where the presence of an outer swirler ring improves the performance, enhancing the rotation of the air flow. It also reduces the axial velocity, resulting in a recirculation of a fraction of the droplets closer to the exit of the nozzle. Arkhipov et al. [25] numerically studied the influence of swirling oxidizer co-flow characteristics on liquid fuel combustion, showing the combustion zone shift with the increasing swirl intensity. A recent numerical study of fuel oil combustion in an industrial furnace by Bonefacic et al. [26] showed the major effect of highly swirling flows for a complete combustion.

The mixing of fossil diesel with different alternative fuels, such as fatty acid methyl esters (FAME, commonly referred to as biodiesel), butanol, hydrotreated vegetable oil (HVO, a synthetic diesel fuel), and so on, will affect the combustion process in the burner. For example, different fuels generally have different physical properties, particularly different kinematic viscosity, which profoundly influences the injected liquid spray characteristics and thus the combustion performance [27–29]. A higher kinematic viscosity suppresses the shear-layer instabilities, responsible for the break-up of the liquid fuel into droplets in the spray [30]. Other important properties are the chemical composition of the fuel, directly affecting the diffusion of fuel molecules after evaporation and the chemical kinetics of the combustion [31], and the heating value, possibly reducing the flame temperature [32]. In simulations of a dual blend of iso-octane and n-heptane, Wu et al. [33] showed that at high co-flow temperature, a difference in time of ignition occurs, with iso-octane igniting before n-heptane, mainly determined by different vaporisation and diffusion rates. At low co-flow temperatures, the opposite was observed, with ignition of n-heptane occurring before iso-octane, due to a slower vaporisation and lower activation energy required for the initial deactivation reaction.

The level of pollutants, such as PAH, CO, hydrocarbons, and NOx, must be avoided during combustion, particularly NOx formation, normally formed in the high-temperature zones of the burner. To avoid NOx formation, a homogeneous, well-mixed combustion process is desired, achieved by an optimized swirl configuration, as demonstrated by Johnson et al. [34]. A previous study [35] reports on NOx concentrations as a function of burner swirl number, concluding that rapid droplet evaporation and long residence time reduce the NOx formation. Lower NOx and CO concentrations were reported by Ling et al. [36], using a combustion configuration consisting of swirl burners with Y-type atomizing nozzles and air staging, over-fire air, and flue gases recirculation.

Today, computer simulation is essential for the analysis, understanding, and description of the combustion process for burner design. Computer simulations couple a number of sub-models, such as turbulence–chemistry interaction, heat and mass interaction between discrete and continuous phase, radiative heat transfer, NOx, sulfur oxides (SOx), and soot formation. These sub-models are based on different theoretical models, each with a complexity depending on the combustion process to be described. The different process steps to be modelled are related to the fuel evolution mechanism including the transformation steps; namely, liquid film formation, sheet break up, atomization into droplets, and evaporation of droplets. These steps depend on nozzle geometry and transport phenomena in reacting flows. Advances of theoretical models describing the liquid fuel vaporization, dispersion, transport, and combustion are readily found in a number of review papers [37–39]. Jenny et al. [37] provided a comprehensive review of computational models relevant for turbulent dilute spray combustion, analyzing the properties of the general modelling approaches and combustion models. They concluded that further work is necessary for the development and experimental validation of computer models for droplet collision, breakup, dispersion, and mixing. Chiu [38] summarized different droplet theories and their applications and bottlenecks in liquid spray combustion. Sirignano [39] reviewed recent advances in droplet array vaporization and combustion theory and computer modelling, including the understandings in the field of transient convective combustion of droplet arrays.

The objective of the work was to increase the understanding of the combustion processes inside a non-premixed prototype 6 kW diesel burner as a core element in vehicle heating applications. This includes determining how key parameters, such as geometrical components of the burner and the nozzle, as well as the air diffuser velocity components, affect the performance, realizing a combustion process free of hydrocarbon and CO. Another objective was to enable the development of better burner configurations; facilitating scale-up capabilities; and injection of different fuels, including various qualities of fossil diesels, bio-diesels, gasoline, and ethanol.

We addressed these objectives by developing a baseline non-premixed combustion model and a pressure swirl jet module to simulate the processes of combustion and liquid fuel injection from the nozzle in the burner. To facilitate a deeper understanding of the influence of different geometrical elements on the burner performance, a stepwise modelling approach was adopted. The baseline

model was compared with experimental results for verification, and thereafter used in modelling of parameters affecting the burner performance.

Modelling of non-premixed burners is commonly performed for applications such as burners for gas turbines, large scale oil burners, and internal combustion engines [11,26,40]. To the best of our knowledge, we believe that this is the first work using an advanced numerical modelling tool to analyze and identify key parameters for design and optimization of small-scale non-premixed diesel burners for heater application. The developed model was verified against experimental data obtained with a real 6 kW diesel burner.

2. Materials and Methods

2.1. Modelling

In the modelling, the basic geometry of the commercial prototype heater was a cylinder with a volume and diameter of 0.32 L and 60 mm, respectively. As discussed in the introduction, there are spatial limitations for overall size of the heater in light duty vehicles and outer dimensions of the burner are fixed. A 3D sectional view of the burner with internal elements is presented in Figure 1 for easier understanding of the burner configuration. The modelled geometry was based on a two-dimensional axisymmetric model. The two-dimensional geometry file can be found in two formats, 'Geometry 2D.agdb' and 'Geometry 2D.igs', in the Supplementary Materials, for more details on the detailed dimensions and for modelling purposes. The air flow, which enters from a swirler air diffuser, could be assumed to be axisymmetric with a good approximation [24]. Calculations were applied according to the steady time solver.

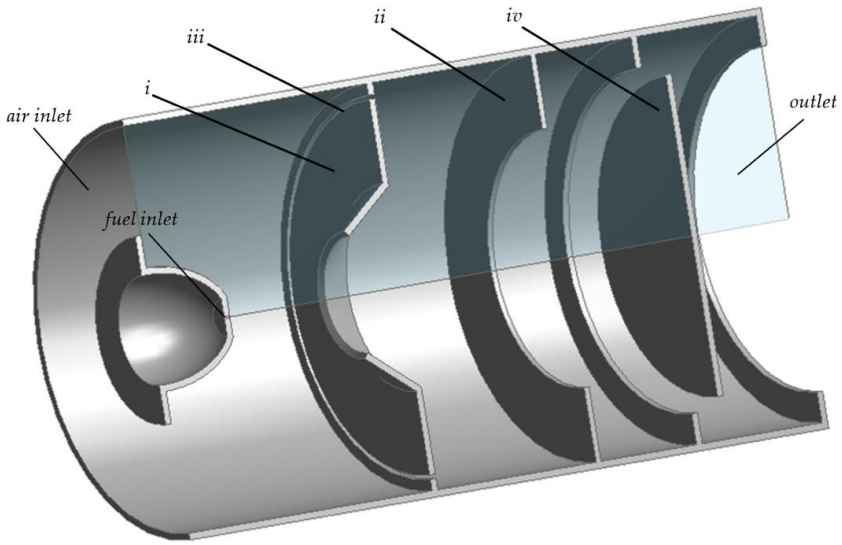

Figure 1. Three-dimensional sectional view of the burner. i: Ring cone; ii: ring cup; iii: slit; iv: mixing plate.

ANSYS Workbench 18.0 [41] was used to prepare and generate the geometry and the mesh. The physics simulations were performed using the ANSYS Fluent 18.0 software in parallel processing mode with seven processors on local memory.

Several factors could have disturbed the overall solution accuracy [42]. Different sources of errors were avoided during the modelling. For example, rounding-off errors, iteration errors, and solution errors were handled by using a high processing power computer and adequate data rounding; recalculating results at higher iterations convergence; and calculating at different grid qualities, including a super refined mesh. The calculation net was defined and generated for a high mesh quality, enabling coverage of all reaction dynamics in the fluid zone. In the pre-study calculations, the mesh was refined several times to ensure that injected liquid and vapour penetration were independent of

the grid. The results were also compared for the gas composition, NOx concentration, and temperature profiles among different smother meshes to decide where the results do not change by the further refinement. The mesh consisted of 74,000 cells and 150,000 faces. Mesh metrics showed a skewness of 0.11, an excellent value; an average orthogonal quality above 0.85, close to the best value of 1; and an average element quality of 0.90, close to the perfect element quality of 1. The number of computational parcels of injected particles was kept high at 300 streams, so the liquid length and pattern were not influenced by this computational parameter. However, the calculation time was almost doubled for every 100 particle streams increase. A view of the mesh is shown in Figure 2.

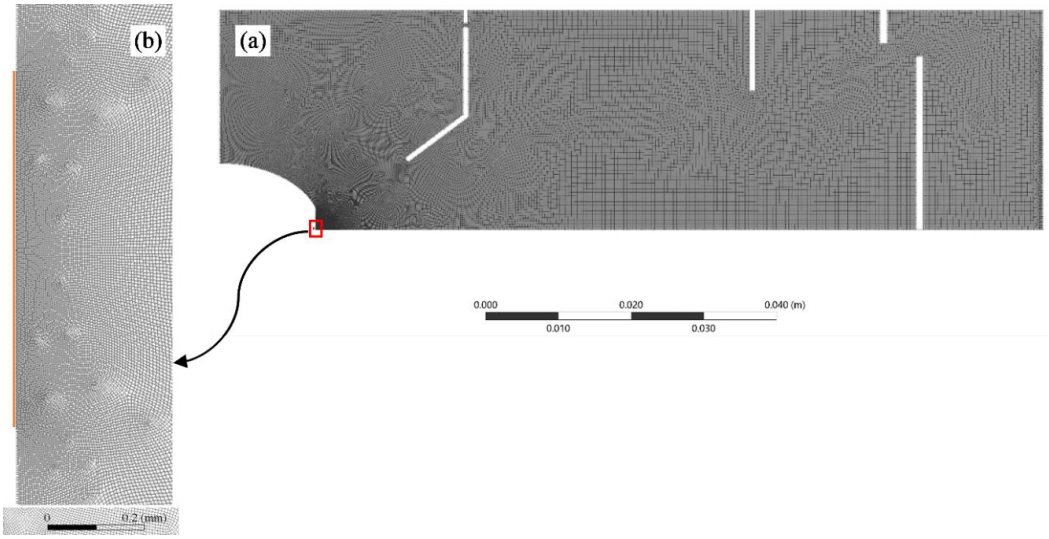

Figure 2. (**a**) View of the mesh of the burner used in 2D axisymmetric model (half of the burner geometry), including nozzle for inlet gas, ring cone, ring cup, and the mixing plate; (**b**) closer view of the refined mesh near the nozzle outlet.

2.2. Model Settings

The following model settings were applied.

2.2.1. Flow

Although pre-analysis of the process for fuel jet showed that the fluid was in the laminar momentum flow at the inlet, the flow was turbulent during combustion. A realizable k-epsilon turbulent model with standard model constants was applied for the turbulence [43]. This viscous model is a semi-empirical turbulence model widely used in industrial flow and heat transfer simulations [44].

2.2.2. Chemical Reaction Model

The probability density function (PDF) approach was applied to predict the flame and the combustion processes [45]. This is a standard method for modelling transport in non-premixed combustion systems and is available in Fluent. The density of the gas mixture in the reaction zone was predicted by PDF, specific heat through the mixing law, and thermal conductivity and viscosity by piecewise linear functions. The absorption coefficient of the gas was calculated from the gas mixture using the weighted-sum-of-grey-gases model (WSGGM). The rich flammability limit constant was set to the optimum value of 0.1, in accordance with the lowest of modelling errors compared with experiments reported in the literature [46].

The model is a non-premixed combustion, which includes diffusion of species at the inlet. Chemical equilibrium state relations were chosen to account for the intermediate species generated and disappearing during the combustion reactions. The maximum number of species in the reactions was set to 41, which is a moderate number compared with highly complex models, which have 110 species,

because it was investigated in the ERC-PRF mechanism [47]. After the look-up tables were generated, the number of species in the reactions was either 22 or 32 in different simulations of the present study. The PDF approach calculates the local mixture fraction to decide whether it is a rich or lean area, and whether it is mixed or unmixed. Species concentrations were then derived from the predicted mixture fraction. Moreover, non-adiabatic energy treatment was chosen for the radiation effects of wall boundaries, which affected the thermochemical equilibrium and the temperature through changes in the enthalpy.

The evaporated fuel was ignited by setting a high initial temperature in the model, where in the experiments, a glow plug was used for ignition.

2.2.3. Radiation

The P1 radiation model is identified as the most popular model considering heat radiation in combustion CFD modelling [48,49]. The P1 model requires entering the absorption coefficient of the flowing gas and the internal emissivity of the grey walls. The scattering coefficient was set to zero, because no particles were considered to exit with the exhaust gas.

2.2.4. Droplet Formation and Evaporation

Several industrial suppliers create different nozzles with hollow or full cone patterns of spray and with different spray angles [50–52]. The nozzle used in this study was a pressure-jet swirl with a spray angle of 60°. Usually, a two-dimensional modelling by ANSYS Fluent software for many of the fuel injector types results in a hollow cone spray. However, it is possible to model a full cone spray by utilizing a pressure swirl atomizer, where a mist of droplets from the atomizer fills the spray cone and no air penetrates the liquid jet [53]. A discrete phase model was used to track the droplets in a Lagrangian approach. This approach was adapted from Schmidt et al. [54] for the film formation phase and from Senecal et al. [55] for the film breakup and atomization in ANSYS Fluent [56]. The diesel–air injection module was used for the physics of the two-phase flow of droplet formation and evaporation; it is available in Fluent. The physics included in the particle model [46,53] are as follows:

- Particle radiation interaction to account for the radiation heat transfer to the particles.
- Temperature-dependent latent heat to include the effect of droplet temperature on latent heat.
- Two-way turbulent coupling to enable effects of change in turbulent quantities due to particle damping and turbulent eddies.
- Thermophoretic force to consider the effects of the thermophoretic force on the particle trajectories, or the force in the direction opposite to that of the gradient in particles with small temperature gradient.
- Saffman lift force to include the lift due to shear forces.
- Coupled droplet and combustion calculations to enable the solution of the corresponding equations, using a coupled ordinary differential equation (ODE) solver with error tolerance control for both droplet and combustion.

2.2.5. Nitrogen Oxides (NOx) Formation

Thermal NOx formation was selected as the dominant mechanism. Calculations were based on the Zeldovich mechanism [57] integrated in Fluent. The extended mechanism includes production of nitrogen oxide from three main reactions: between oxygen atoms and nitrogen molecules ($O + N_2 \leftrightarrow NO + N$), oxygen molecule and nitrogen atoms ($O_2 + N \leftrightarrow NO + O$), and hydroxyl radicals and nitrogen atoms ($OH + N \leftrightarrow NO + H$). The concentration of radicals was predicted from the mass fractions of the combustion model. In addition to thermal NOx, the possibility of prompt NOx formation, occurring mostly in rich flames, was calculated according to Backmeier et al. [58], a feature included in Fluent. As the organic nitrogen content in the diesel is almost zero, fuel NOx formation was not reflected in the calculations.

2.2.6. Solver Settings

The pressure-based segregated algorithm SIMPLE was applied, which is a standard algorithm and is recommended for more complicated flows that involve turbulence and combustion [59].

The second-order discretization was chosen to achieve a higher accuracy in the results, even though the calculation time was increased by about three times.

2.2.7. Boundary Conditions

The fuel flow rate was equivalent to a produced power of 6 kW. The lower heating value (LHV) of the fuel was 43.1 MJ/kg, and n-decane ($C_{10}H_{22}$) was considered as the mean molecular formula for the diesel fuel.

Adiabatic boundary conditions were taken for all the cylinder walls throughout the burner design progression (Section 3.1). However, in the optimization (Section 3.2), a heat transfer function for the walls was added. The convective heat effect outside the burner cylinder was taken into account as a free fluid stream and calculated through Nusselt correlations by Dittus, P.W. and Boelter [60]. The average fluid temperature and the overall heat transfer coefficient were 40 °C and 279 W/m^{2}K, respectively, to consider the overall heat exchange between the walls and the fluid.

The radial and tangential components of the inlet air velocity were not measured by experiments but were calculated through geometrical components of the air diffuser [61], according to the theoretical equation for swirl number:

$$Swirl\ number = 2/3 \left[\left(1 - (D_{hub}/D_{sw})^3 \right) / \left(1 - (D_{hub}/D_{sw})^2 \right) \right] \tan\theta \quad (1)$$

The vane diameter, D_{hub}, and the swirler diameter, D_{sw}, were constant in all cases, so that $\frac{D_{hub}}{D_{sw}} = 0.59$. The hub-to-tip ratio was kept constant (Figure 3) in order to keep the fan size performance constant along the cases. The vane angle, θ, was 45 degrees. Because of a lack of measurement data for the radial distribution of swirling velocity components at the exit of the swirler, a constant distribution was assumed at the model inlet boundary, based on a plug flow assumption. However, this assumption deviates for high degrees of swirl numbers (>0.7) in which a larger portion of axial and tangential components can exit at the outer edge of the boundary [61]. The swirl vane efficiency is assumed to be 100% in the present study. It is adopted from comparing air outlet angle with blade angle [61], approximated equal as the pitch/chord ratio of the swirler in this work is 0.51.

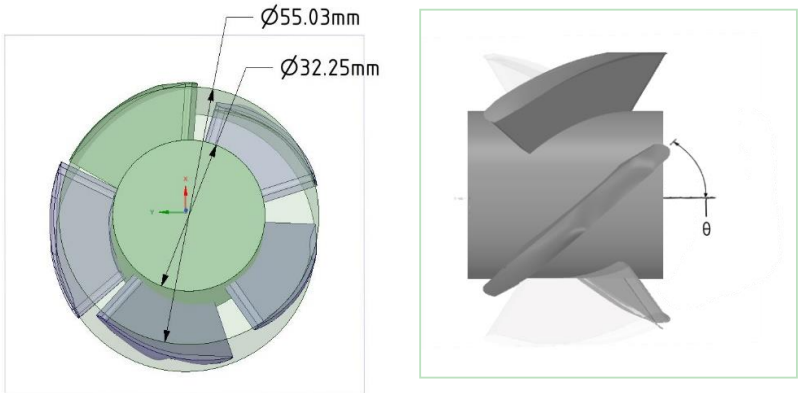

(**a**) (**b**)

Figure 3. Drawing of the air diffuser displaying the diameters and the vane angle: (**a**) top view; (**b**) side view.

2.3. Experiments

The combustion experiments for model verification were performed in a test rig, as illustrated in Figure 4. The air flow to the heater was controlled by adjusting the speed of the fan motor, using

an electronic control unit additionally connected to a wide-band lambda sensor (Bosch LSU 4.9), measuring the air-to-fuel ratio in the exhaust. The lambda sensor measured the excess oxygen online in the exhaust gas and adjusted the power of the fan to achieve a target lambda for each experiment in the range of 1.3 to 1.45. The uncertainty of the lambda sensor in this range is 0.03 [62].

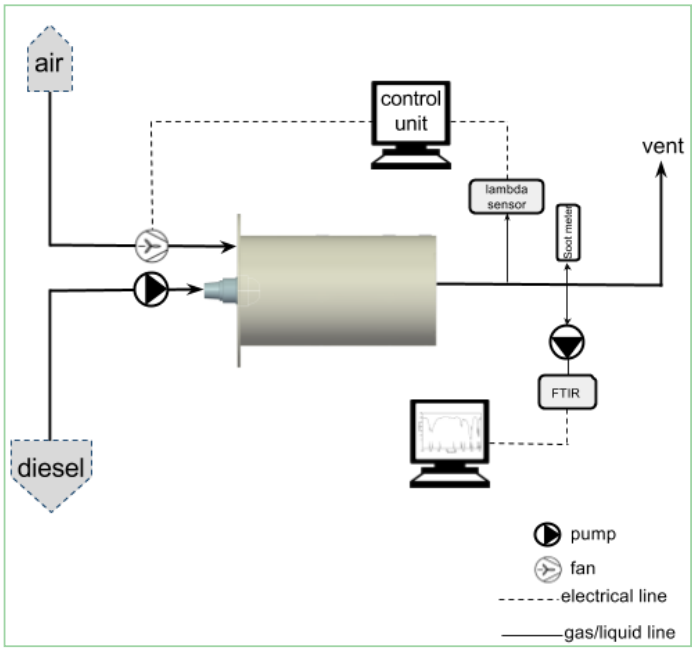

Figure 4. Simplified experimental setup. FTIR—Fourier-transform infrared spectroscopy.

Diesel fuel was pumped to the heater according to a targeted heating power in the range of 5.75 to 7 kW (the measured fuel flow rates range from 8 to 9.74 g/min). A heated probe was inserted into the exhaust tube to sample gas for gas analysis by means of a Fourier-transform infrared spectroscopy (FTIR) unit model MultiGas Analyser 2030. All of the gaseous compounds, except for the diatomic symmetric molecules H_2, O_2, and N_2, were analyzed and monitored via the software MKS MG2000 connected to the FTIR. The sensitivity of the measurements is between 10 and 100 ppb for the different gases [63]. Unburned gas measurements in the exhaust gas by FTIR spectroscopy method are described in the literature [64]. The presence of soot was measured by means of a Testo 308 digital smoke meter. The soot measurement range, resolution, and accuracy were 0–6, 0.1, and ±0.2 smoke number, respectively. The correlation between smoke number and soot concentration mg/m^3 is found in several references and manuals, such as the work of [65]. Experimental data and flow rates for the 6 kW heater are tabulated in Table 1. The experiments were repeated for five heating powers, 5.75, 6, 6.25, 6.7, and 7 kW. Four different lambda, 1.3, 1.35, 1.4, and 1.45, were tested for each of the mentioned heating powers.

Table 1. Input data and flow rates for the 6 kW heater experiments. LHV—lower heating value.

Diesel fuel LHV (MJ/kg)	43.1
Fuel injection temperature (°C)	10
Ambient air temperature (°C)	10
Fuel injection pressure (kPa)	400
Fuel flow rate (g/min)	8.35
Lambda	**Air Mass Flow Rate (g/s)**
1.3	2.713
1.35	2.817
1.4	2.922
1.45	3.026

3. Results and Discussion

3.1. Development of the Baseline Model

The stepwise model development started with combustion simulations using an empty cylinder configuration; the model was subsequently improved in three steps by adding geometrical components such as a cone, a ring, and gas channels.

The stepwise developed models are presented by geometries A, B, and C, where C is the baseline geometry verified against experimental results. Model results in terms of profiles of fuel mass fraction or vapour fuel penetration profile and contours of temperature are presented in Figure 5 for these three geometries. For an easier following of the geometry, please see the 3D sectional view of the burner and internal elements in Figure 1.

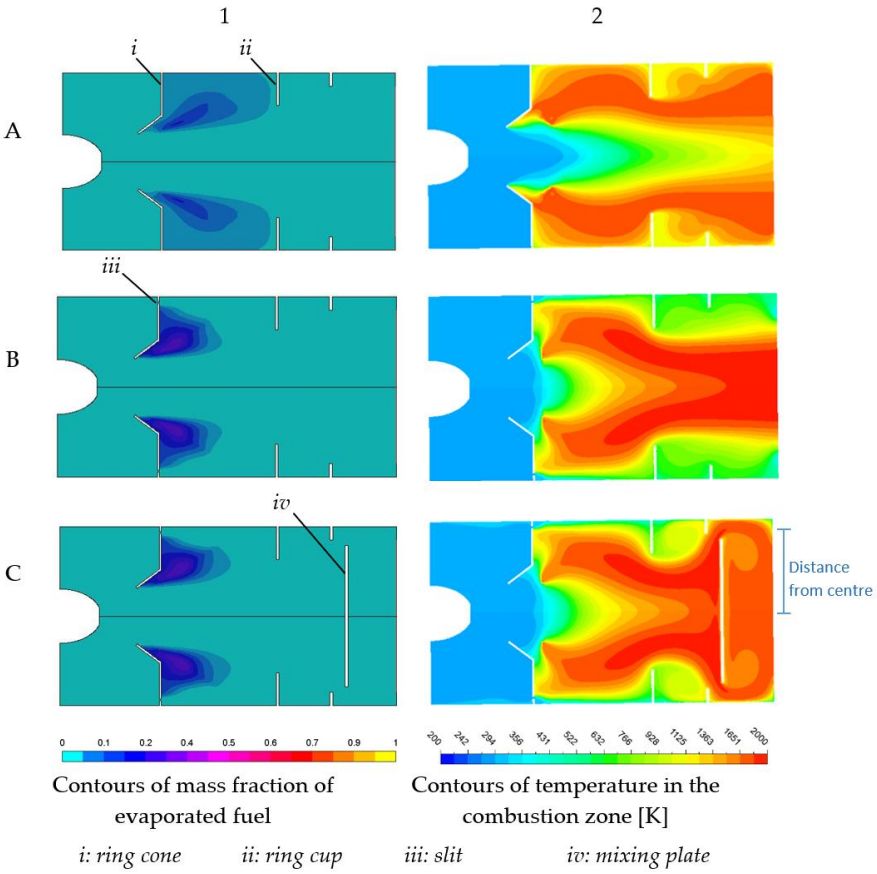

Figure 5. Contours of mass fraction of fuel (**column 1**) and temperature (**column 2**) for three geometry cases (**A–C**).

As shown in Figure 5(A1), the injected fuel was mainly accumulated after the ring cone for geometry A and was widely distributed toward the walls and the ring cup. The combustion started from the outer fuel accumulation area as shown in the temperature profiles (Figure 5(A2)). By adding a slit on the ring cone, as in case of geometry B (Figure 5(B1)), fuel was forced toward the center by the stream of air passing through the slit. Thus, the size and shape of the fuel accumulation area was concentrated to a denser area toward the center, causing the flame to be shaped mainly between the ring cone and the cup cone (Figure 5(B2)). Consequently, the trace amounts of unburned fuel at the outlet decreased from 37 ppm in geometry A to 8 ppm in geometry B. To further improve the combustion, an additional modification in the form of a mixing plate was introduced before the outlet, as shown in geometry C, Figure 5(C1). A closer view of the velocity streamlines around the mixing plate is provided in Supplementary Figure S1. Recirculation bubbles after the mixing plate and flow

separation on the edges of the mixing plate are observed. The flow pattern modelled in this study is in line with previous numerical studies about flow around a flat plate [66,67]. The main mixing effect takes place in the area between the plate and the burner wall. Introducing the mixing plate not only forced the fuel growth area and thus the flame a little more to the center, but also resulted in full combustion with no traces of fuel left in the outlet gas. Furthermore, the mixing plate resulted in a highly uniform outlet gas composition and temperature. For comparison, the gas temperature distribution along the outlet for all three geometry cases is shown in Figure 6. The figure illustrates the highly uniform gas temperature in the case of C. Standard deviation for gas temperature along the outlet was 211 and 582 K for cases A and B, respectively, where it decreased to 92 K for geometry C, in keeping with the higher uniformity of the gas condition and composition for geometry C. This was confirmed with uniformity index [68] results for gas temperature at the outlet boundary, which were 0.754 and 0.968 for cases B and A, respectively, and 0.973 for geometry C.

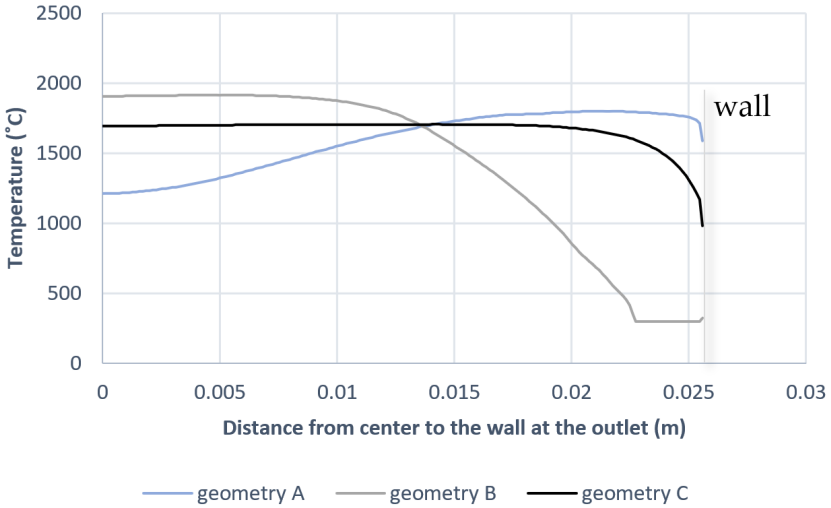

Figure 6. Temperature distribution along the outlet boundary (shown in Figure 5(C2)) for three geometry cases; A, B, and C.

The experimental conditions for the model verifications are stated in Table 1. The outlet gas analysis was carried out as described in Section 2.3 (Experiments).

The model errors, the difference between model results and experimental results, were compared at lambda values of 1.3, 1.35, 1.4, and 1.45 for geometry C, which is the same burner geometry used in the experiments. In all cases, the main components of the outlet gas were predicted by the model with high accuracy, verifying the model versus the experimental measurements. This was exemplified with the outlet gas composition for the case with lambda of 1.3, as presented in Table 2, where the average accuracy of the model results for the four main components, N_2, O_2, CO_2, and H_2O was 0.25 mol%. In addition, the right column represents the expected gas composition obtained using a theoretical full combustion calculation [69]. The experimental results were also close to the theoretical composition, with a similar accuracy of 0.23 mol%.

The main components accounted for 99.94% of the exit gas. A comparison of the remaining fraction in the experimental results showed 4 ppm of unburnt diesel fuel; around 2 ppm of each of the lighter hydrocarbons ethylene, propane, and propylene; 482 ppm of CO; and 58 ppm of NO. In the modelling, the results displayed a negligible amount of hydrocarbons, displaying a more complete combustion. Furthermore, a lower CO result was expected from the model (58 ppm, compared with the 482 ppm for the experiments) because the model estimated 0.03% or 300 ppm higher CO_2 compared with the experiments. The emitted amount of the pollutant CO, 482 ppm, is possibly not yet critical because of the regulations of emissions from heating systems in the passenger cars for the moment,

but the design of future burners must consider stricter regulations for both the small burners, as for this work, and for scaled-up cases in the future.

Table 2. Outlet gas composition for the main components for model, experimental results (6 kW burner, lambda 1.3), and theoretically calculated results.

Component	Model	Experimental	Theoretical [1]
N_2 (%)	74.71	74.88 [2]	74.83
O_2 (%)	4.62	4.91	4.56
CO_2 (%)	9.83	9.80	9.81
H_2O (%)	10.81	10.35	10.79

[1] Gas composition through the complete combustion reaction: $C_xH_y + (x + \frac{y}{4})(O_2 + 3.785N_2) \rightarrow xCO_2 + \frac{y}{2}H_2O + 3.785(x + \frac{y}{4})N_2$. [2] The nitrogen was calculated according to the lambda measurement of the oxygen in the input air.

Regarding modelling of soot formation, the model shows minor amounts of soot, as shown in Figure 7, which were formed in the low air–fuel ratio areas between the two cones. However, as shown by the results, the soot oxidized back immediately with no traces of soot at the outlet. This was confirmed by the experimental results for soot at the outlet gas, where no soot was detected.

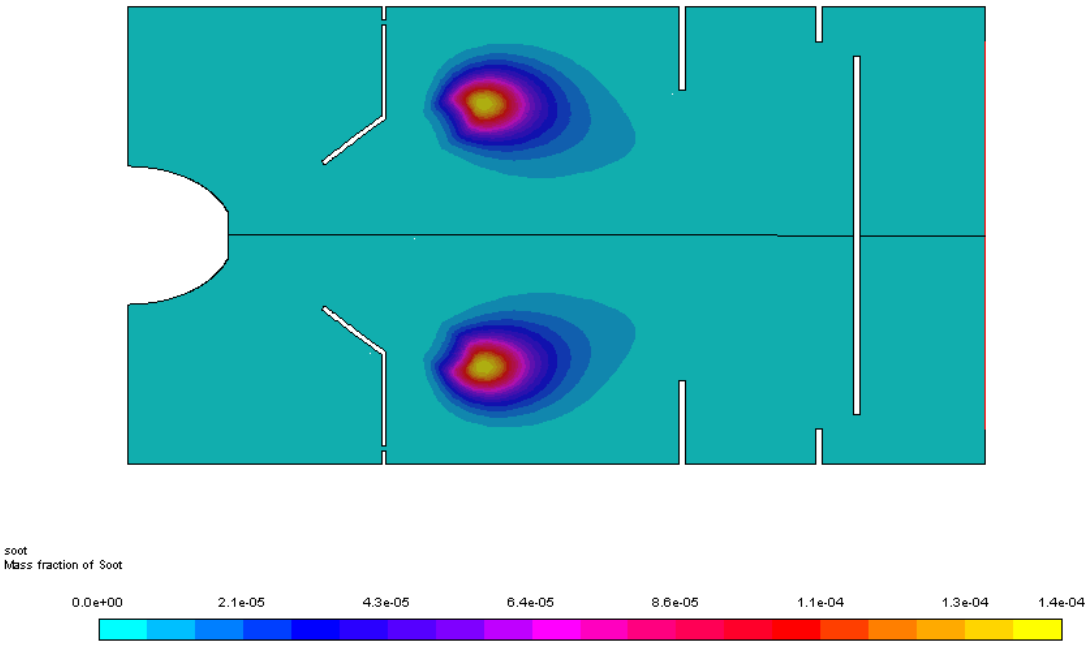

Figure 7. Tracking soot formation and profiles of soot mass fraction in the combustion zone, geometry C.

NOx of 10 ppm was predicted in the model, which was less than the 58 ppm observed in the experiments. As mentioned in the methodology section, thermal NOx is the dominant mechanism in this process. Previous studies in the literature also confirm that thermal NOx results from decoupled calculations are under-estimated compared with experimental results [70]. Calculation of NOx, which was decoupled, could be performed as coupled to the combustion modelling; however, the computer processing times would be much longer. To compare coupled and decoupled NOx calculations, we performed calculations with both methods for one case. The result showed that the coupled method had 30% higher NOx results than the uncoupled modelling. Therefore, it is recommended to apply coupled NOx calculations, especially if studies of NOx emission are the core of the simulation.

Another possible reason for under-prediction of NOx in the model could come from a minor uncertainty about the nozzle diameter, as the detailed design of the nozzle geometry was confidential. The diameter was estimated by the optical method to be 0.3 mm and this value was used in the model. Droplet size could affect temperature profile, which affects the thermal NOx formation. According to

theoretical and empirical studies on the droplet size, there is an inverse relation between the nozzle diameter (D) and droplet diameter, such as, for instance, in the Hermon's equation [71,72].

The influence of the nozzle diameter on the droplet evolution and combustion process is discussed in Section 3.2.3.

3.2. Optimization

The optimization aimed at utilizing the verified baseline case C model to improve the design in general. Modelling can also be used to improve the design for a specific reason, such as fuel flexibility, scalability, and so on.

In this section, after the model was verified, the possibilities of improving the geometry of the burner were tested in three ways: relocation of the ring cone, effect of the air diffuser vane angle represented by the velocity components in the air inlet boundary condition, and varying the nozzle diameter.

First, the impact of changing the location of the ring cone was tested. This ring, which is the first one that the gases approach in the burner, affects the oxygen flow pattern and the fuel pattern. The ring cone plays a more significant role than the other geometrical elements inside the combustion zone. To determine the most optimized location for the ring cone, five different distances (a to e, Figure 8a) were modelled using the same input data as in Table 1.

Figure 8. Burner design optimization: (**a**) cases for relocating ring cone (location c is the same as the baseline case C); (**b**) changing the air inlet swirl velocity (vane angle in the experimental case was 45°).

Next, the swirl component of the inlet air velocity, which represents different vane angles, was varied to find the best range for the air swirl velocity for the burner. The vane angle of the air diffuser was varied between 25 and 65 degrees (Figure 8b) to evaluate the effects on flow mixing and fuel particle trajectory. The hub-to-tip ratio was kept constant, as mentioned in Material and Methods (Section 2).

Finally, the nozzle diameter was varied between 0.1 and 0.3 mm, which is a typical range for diesel injection nozzles [73–75].

3.2.1. Ring Cone Distance

As visualized in Figure 9(d1,e1), the fuel evaporated more in the axial direction when the ring cone was far from the nozzle. This resulted in a more pronounced flame in the axial direction, causing the main combustion to occur at the end of the second zone and close to the mixing plate and outlet, as illustrated in Figure 9(d2,e2).

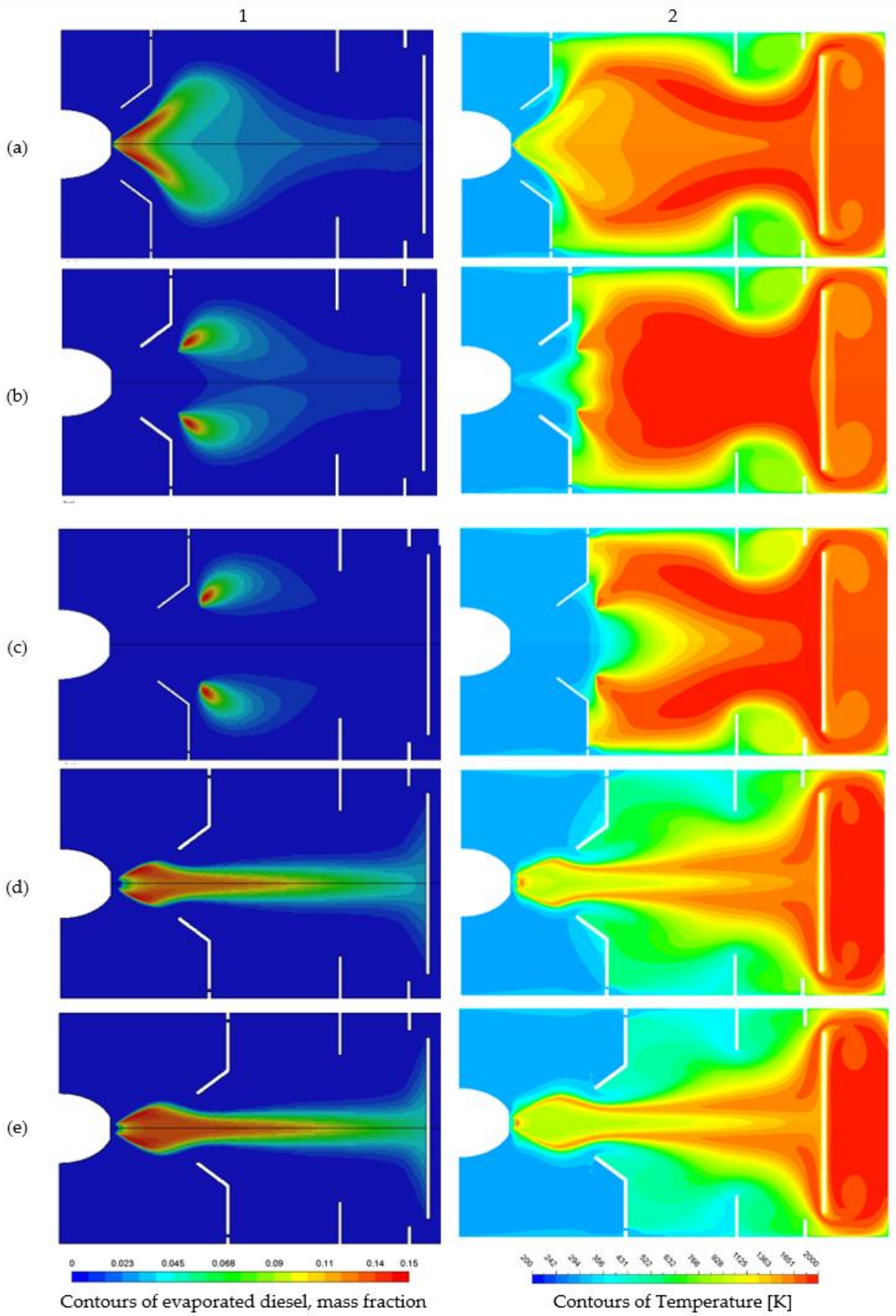

Figure 9. Contours of evaporated fuel (**column 1**) and temperature (**column 2**) for cases (**a**–**e**) of relocating the ring cone. In case (**c**), the ring cone is at the same distance from the nozzle as in the baseline case (C) in Section 3.1.

If the ring cone is located too close to the nozzle, the fuel evaporated in a cone shape pattern close to the nozzle (Figure 9(a1)) in a large area. In this case, the highest flame temperature is relatively close to the second ring, implying that the combustion had started closer to the nozzle, but was not completely combusted before the second ring (Figure 9(a2)). Cases b and c, Figure 9, showed the best performance among the cases, suggesting a more secure operation of the burner. Therefore, if the ring cone is moved 5 mm closer toward the nozzle (case b), compared with the baseline case C, improved flame center location and temperature profiles are suggested.

When the location of the ring cone is changed, the radial component of the velocity changes because the gas is forced toward the center as it approaches the ring cone. Therefore, in cases d and e, where the ring cone is far from the nozzle, the gas is not forced, and the gases have a higher axial velocity, as can be seen in the velocity profiles in Supplementary Figure S2. This is in agreement with previous results by Chong and Hochgreb [23], analyzing the influence of geometry components such as burner walls on flow fields, velocity components, and recirculation zones. In cases b and c, the gas was forced toward the middle of the cylinder, and hence the air and fuel mixed earlier and combusted in the center of the burner. In case a, where the ring cone is significantly closer to the nozzle, the gases are forced toward the middle, but they then shifted toward the walls because, although the mixing is good, the radial velocity was too high. It is concluded that case b is slightly better than case c, used in the verification experiments. Comparing NOx formation for the two cases b and c, the average mole fraction of NO of case b at the outlet stream has a slightly lower emission of 8.9 ppm, compared with case c with 9.2 ppm.

3.2.2. Air Swirler

The effects of the air swirler arrangement on the air flow components and thus on the droplet trajectory were studied for five sets of velocity components, V1 to V5, representing swirl numbers ranging from 0.38 to 1.74. The tangential velocity component, calculated using Equation (1), increases for each case as shown in Table 3. The profiles of tangential velocity for each case are shown in the first column of Figure 10. In all the air swirler cases, the location of the ring cone was as in the baseline case C.

Table 3. Velocity components for inlet air stream at different swirl cases, geometry C.

Type of data	Parameter	V1	V2	V3	V4	V5
Input data	**Velocity components**					
	Axial	1	1	1	1	1
	Tangential	0.47	0.70	1.00	1.43	2.14
	Radial	0.21	0.21	0.21	0.21	0.21
	Geometrical components					
	D_{hub}/D_{sw}	0.59	0.59	0.59	0.59	0.59
	θ (degree)	25	35	45	55	65
	Swirl number	0.38	0.57	0.81	1.16	1.74
	Vane angle (degree)	25	35	45	55	65
Results	Liquid length [1] (mm)	70	67	61	48	25

[1] Liquid length: the axial position of leading particle, as illustrated for all cases in Figure S3, in the Supplementary section.

As the swirl number increases from V1 to V5, it affected the liquid penetration profile because the axial velocity component decreased, and the droplets had to travel a shorter distance along the burner. The particles evaporation and recirculation zone formed closer to the nozzle. This is illustrated by the liquid length, defined as the axial position of leading particle [73] in Table 3, decreasing from 70 mm in case V1 to 25 mm in case V5. Furthermore, the profiles of particle trajectory and fuel evaporates are affected. The particle trajectories, shown as grey dotted points in column 2 of Figure 10, present the location of particles before evaporation. The differences in droplet location are in agreement with the

observed decrease in liquid length. The profiles of evaporated fuel, displayed in column 3 of Figure 10, show changes in the vapour penetration profiles in response to increasing the swirl intensity. Case V5 presents a stronger recirculation zone, compared with case V3, the baseline case; however, the vapored fuel is further away from the ring cone.

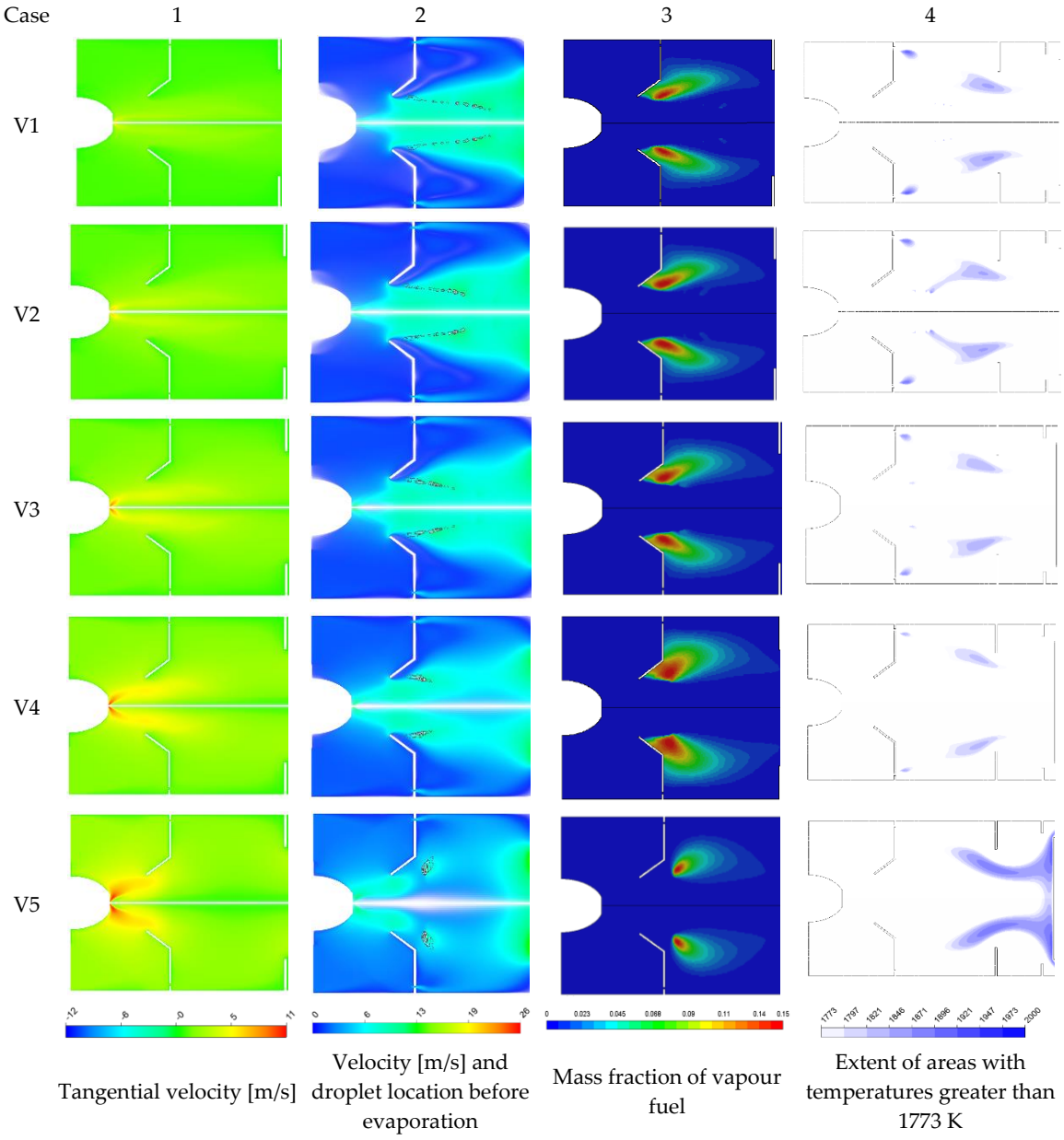

Figure 10. Simulation results for effect of increasing the inlet air swirl number from V1 to V5; (**column 1**): contours of tangential velocity; (**column 2**): contours of velocity together with lines presenting the droplets before evaporation; (**column 3**): contours of mass fraction of evaporated fuel; (**column 4**): contours of regions with high gas temperatures. The figures are zoomed in to show a closer view of the first sections of the combustion zone.

The temperature profiles appear more centered for cases V3 to V5, shown in Supplementary Figure S4. The temperature profiles for the swirl cases V1 and V2 are more axially developed, as is expected from the velocity profiles and the particle breakup profiles, illustrated in column 2 of Figure 10. V3 to V5 have better liquid and vapour penetration, creating strong recirculation zones and stabilizing the temperature profiles in the center, compared with V1 and V2. Cases V1 and V2, with swirl numbers

of 0.38 and 0.57, respectively, do not have efficient recirculation zones close to the ring cone. This is in line with previous literature findings stating that recirculation zones are usually formed for swirl numbers above 0.6 [76], as illustrated by swirl cases V3 to V5 in the present study. Conclusively, the air diffuser swirl used in the baseline case C, with a vane angle of 45 degrees, can be increased to 65 degrees to improve the combustion. However, as mentioned in Section 2.2.7 in setting uniform boundary velocity components, the high swirl number could impact the radial distribution of the velocity components, and result in a deviation from a constant radial distribution for case V5.

Changing the swirl degree affects the turbulence mixing and the recirculation, as well as the lean and rich areas and high-temperature regions, which affect thermal NOx formation rates and extents. Column 4 of Figure 10 displays areas with temperatures greater than 1500 °C (1773 K), where nitrogen oxides may be formed if oxygen is available. The high-temperature zone grows and moves further to the left with an increase in swirl number. Specifically, case V5, which had the highest swirl number, had an expanded area of high temperatures. The shrinking and subsequent expansion of the high-temperature area (cases V2 to V5) suggests that there would be a minimum of thermal NOx emission related to increasing the swirl number. The effects of swirl number on NOx formation were investigated by Johnson et al. [34], comparing the result of two different swirl numbers of 0.5 and 0.73 on the emission products, demonstrating that the case with a lower swirl number had reduced levels of NOx formation. In our case, evaluating a series of cases varying the swirl number, we were able to find an optimized swirl for our burner configuration. NOx emission at the outlet stream is graphed in Figure 11, which shows the minimum emission at a swirl of 0.81. This is important for applications that have a narrow limit on emission of nitrogen oxides, where swirl numbers below 1.16 can be taken as the recommended swirl degrees.

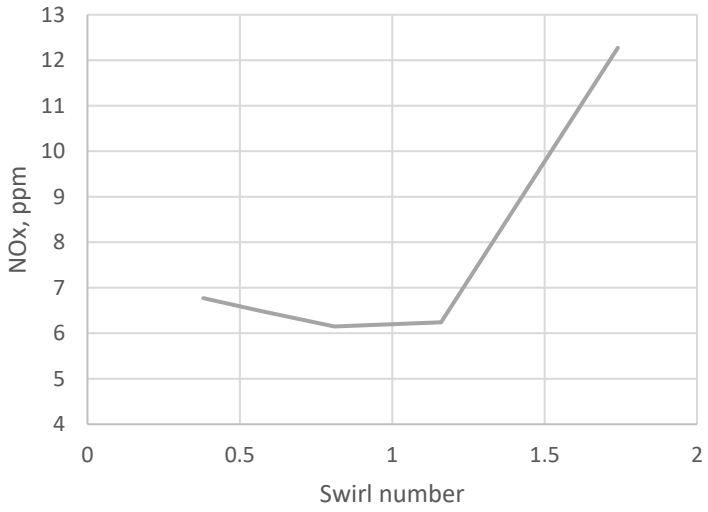

Figure 11. Nitrogen oxide (NOx) at outlet gas versus swirl number of the inlet air.

3.2.3. Nozzle Outlet Diameter

A range of nozzle exit diameters from 0.1 to 0.3 mm were investigated for case with lambda of 1.3, using the same input data as in Table 1. Smaller droplets facilitate fast ignition, while larger droplets take longer to ignite. This is based on the breakup time of sprays that is directly dependent on the nozzle diameter, D, as, for instance, correlated by the Kelvin–Helmholtz (KH) instability model, which shows that the breakup time is μD [74].

A liquid penetration profile and liquid length were tabulated for different nozzle diameters and as Table 4 shows, an increase in the nozzle diameter resulted in a decrease in the liquid length.

Table 4. Liquid penetration track and liquid length versus different injecting nozzle diameters.

Nozzle Diameter (mm)	Particle Trajectory	Liquid Length (mm)
0.10	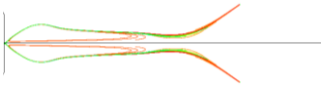	29.2
0.15	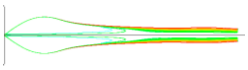	28.8
0.20	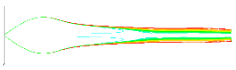	27.9
0.25	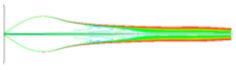	27.7
0.30	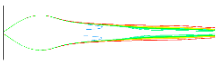	26.0
		

As displayed in the particle trajectory for a small diameter of 0.1 mm, droplets were forced to divert against the walls, and, as shown in the evaporated fuel profiles (Supplementary Figure S5), the vapour fuel was located behind the second ring. This divergence for the small droplets is in agreement with a study by Rimbert and Castanet [53], stating that small droplets are developed following the turbulence in the mixing zone, while the large droplets are mainly governed by classical linear instability. Another consideration here was the liquid film thickness when it first flowed from the orifice. The initial film thickness was in a reverse ratio to the nozzle exit diameter [75]. Hence, for the smaller nozzle diameters, the initial liquid film was thicker, and the sheet breakup took place in the longer lengths, as the other parameters of atomization and air flow were kept unchanged.

In conclusion, having the geometry and lengths of the spray and combustion zones of the burner, by studying the trajectory of the droplets together with fluid dynamics in CFD simulations, it was observed that diameters below 0.15 mm cause diverged droplets. The suitable injection diameter range was detected in range 0.15 to 0.30 mm, leading to a favoured fuel evaporation development and combustion process.

4. Conclusions

The key parameters affecting diesel combustion and their properties were investigated for a 6 kW diesel burner for vehicles heating applications. A non-premixed combustion model and a pressure swirl jet module were developed to simulate the processes of combustion and liquid fuel injection from the nozzle. The model was successfully applied to the burner, predicting the burner performance in comparison with experimental results. The compared main gas composition is in agreement with differences for trace elements and CO and NOx at ppm level, indicating the need for coupled NOx calculations. Soot formation was also tracked and the potential locations for soot accumulation were detected as being between the rings in the zone.

Adding the geometry components piece by piece in the modelling showed the influence of each component. In particular, it displayed the importance of the first geometry item, called a ring cone, which has a high impact on flow streams, on mixing the fuel and air streams, and on the development of the droplets.

The effect of the swirling intensity of the inlet air was investigated for different swirl numbers, significantly affecting the combustion process. The optimum swirl number, above 0.6, for the burner tested and the range of 0.8–1.2, for further optimizing the particle trajectory and the flame location were identified for efficient mixing, particle distribution, and reduced NOx formation.

To identify possible divergent particle vaporization, the influence of the nozzle diameter was studied. A range of diameters was simulated to determine an efficient atomization for achieving a stabilized flame, pointing at a small nozzle diameter to avoid divergent particle evaporation.

Key parameters related to geometrical components of the burner and the air diffuser velocity components are especially important for optimizing the design for scaled-up cases and applying various fuel compositions. The limitations on the burner dimensions in a light duty vehicle affected the range of the design optimizations. Nevertheless, the two-dimensional model developed is robust and can be used for scaling up, such as to 25 kW heaters for buses. The main general findings are summarized as follows:

- A ring close to the nozzle has a high impact on flow streams, on mixing the fuel and air streams, and on the development of the droplets. The distance from the ring cone to the nozzle is essential for the fluid dynamics and the flame location, forcing the gas. A proper ring shape and distance from the nozzle forces the gas toward the center when it approaches the ring cone and, ideally, the air and fuel mix earlier and combust in the center of the burner
- The design of the swirl co-flow is important, especially to achieve low emissions of thermal NOx. Changing the swirl degree affects the turbulence mixing and the recirculation, as well as the lean and rich areas and high-temperature regions.
- A proper nozzle diameter is important to avoid divergent particle vaporization.

Supplementary Materials: The following are available online at http://www.mdpi.com/1996-1073/11/11/2904/s1, Figure S1: velocity streamlines around the mixing plate, Figure S2: velocity rendering results by changing the location of the ring cone, Figure S3: liquid length for different air swirl numbers, Figure S4: contours of temperature profiles for different air swirl numbers, Figure S5: contours of evaporating droplets for the smallest nozzle diameter, Geometry S1: geometry file in Ansys workbench format, Geometry S2: geometry file in IGS workbench format.

Author Contributions: Conceptualization, H.K. and K.E.; Data curation, Z.S.M.; Formal analysis, Z.S.M., H.K., and K.E.; Funding acquisition, H.K. and K.E.; Investigation, Z.S.M., H.K., and R.A.; Methodology, Z.S.M., H.K., R.A., and K.E.; Project administration, K.E.; Resources, H.K., R.A., and K.E.; Software, Z.S.M.; Supervision, K.E.; Validation, Z.S.M., H.K., and K.E.; Visualization, Z.S.M.; Writing—original draft, Z.S.M.; Writing—review & editing, Z.S.M., H.K., R.A., and K.E.

Funding: This research was funded by the FFI for the project 'Katalytisk biobränslebaserat värmarsystem för lätta och tunga fordon' number P40277-1.

Conflicts of Interest: The authors declare no conflict of interest.

References

1. EPA (The Environmental Protection Agency). *Inventory of U.S. Greenhouse Gas Emissions and Sinks*; The Environmental Protection Agency: Washington, DC, USA, 2018.
2. EEA (European Environmental Agency). *Greenhouse Gas Emissions from Transport*; European Environmental Agency: Copenhagen, Denmark, 2017.
3. EEA (European Environmental Agency). *Final Energy Consumption by Mode of Transport*; European Environmental Agency: Copenhagen, Denmark, 2017; p. 12.
4. EIA (U.S. Energy Information Administration). *International Energy Outlook 2017*; U.S. Energy Information Administration: Washington, DC, USA, 2017; p. 143.
5. England, G.C.; McGrath, T.P.; Gilmer, L.; Seebold, J.G.; Lev-On, M.; Hunt, T. Hazardous air pollutant emissions from gas-fired combustion sources: Emissions and the effects of design and fuel type. *Chemosphere* **2001**, *42*, 745–764. [CrossRef]
6. High Heating Comfort at Low Temperatures. Available online: Webasto.com/gb/markets-products/car/heating-systems-for-automotive-industry/auxiliary-heaters/ (accessed on 21 August 2018).
7. Lindström, B.; Karlsson, J.A.J.; Ekdunge, P.; De Verdier, L.; Häggendal, B.; Dawody, J.; Nilsson, M.; Pettersson, L.J. Diesel fuel reformer for automotive fuel cell applications. *Int. J. Hydrogen Energy* **2009**, *34*, 3367–3381. [CrossRef]

8. Lohse-Busch, H.; Duoba, M.; Rask, E.; Stutenberg, K.; Gowri, V.; Slezak, L.; Anderson, D. Ambient Temperature (20° F, 72° F and 95° F) Impact on Fuel and Energy Consumption for Several Conventional Vehicles, Hybrid and Plug-In Hybrid Electric Vehicles and Battery Electric Vehicle. *SAE Int.* **2013**. [CrossRef]
9. Anenberg, S.C.; Miller, J.; Minjares, R.; Du, L.; Henze, D.K.; Lacey, F.; Malley, C.S.; Emberson, L.; Franco, V.; Klimont, Z.; et al. Impacts and mitigation of excess diesel-related NOx emissions in 11 major vehicle markets. *Nature* **2017**, *545*, 467–471. [CrossRef] [PubMed]
10. ICCT (International Council on Clean Transportation). *Final EPA Rule for Renewable Fuel Standard 2014–2016 Volumes*; International Council on Clean Transportation (ICCT): Cainta, Philippines, 2015.
11. Xing, F.; Kumar, A.; Huang, Y.; Chan, S.; Ruan, C.; Gu, S.; Fan, X. Flameless combustion with liquid fuel: A review focusing on fundamentals and gas turbine application. *Appl. Energy* **2017**, *193*, 28–51. [CrossRef]
12. Parking Heaters from the Market Leader. Available online: https://www.webasto.com/fileadmin/webasto_files/documents/international/car/brochure/car-parking-heater-brochure.pdf (accessed on 21 August 2018).
13. Automotive Heaters. Available online: http://www.reformtech.com/en-GB/products/water-heaters-33461313 (accessed on 21 August 2018).
14. Fontaras, G.; Zacharof, N.-G.; Ciuffo, B. Fuel consumption and CO_2 emissions from passenger cars in Europe—Laboratory versus real-world emissions. *Prog. Energy Combust. Sci.* **2017**, *60*, 97–131. [CrossRef]
15. Walnum, H.J.; Simonsen, M. Does driving behavior matter? An analysis of fuel consumption data from heavy-duty trucks. *Transp. Res. Part D Transp. Environ.* **2015**, *36*, 107–120. [CrossRef]
16. Volkswagen A New Standard—An Overview of WLTP for Passenger Cars and Light Commercial Vehicles. Available online: https://www.volkswagenag.com/presence/konzern/group-fleet/dokumente/WLTP_Basic_Knowledge.pdf (accessed on 21 August 2018).
17. Regulation No 122 of the Economic Commission for Europe of the United Nations (UN/ECE)—Uniform Technical Prescriptions Concerning the Approval of Vehicles of Categories M, N and O with Regard to Their Heating Systems. 2010. Available online: https://eur-lex.europa.eu/legal-content/EN/TXT/PDF/?uri=CELEX:42010X0630(08)&from=EN (accessed on 21 August 2018).
18. Lilley, D.G. Modeling of combustor swirl flows. *Acta Astronaut.* **1974**, *1*, 1129–1147. [CrossRef]
19. Syred, N.; Beér, J.M. Combustion in swirling flows: A review. *Combust. Flame* **1974**, *23*, 143–201. [CrossRef]
20. Warnatz, J.; Maas, U.; Dibble, R.W. *Combustion Physical and Chemical Fundamentals, Modeling and Simulation, Experiments, Pollutant Formation*, 3rd ed.; Springer: Berlin/Heidelberg, Germany, 2001; ISBN 978-3-662-04508-4.
21. Tangirala, V.; Chen, R.H.; Driscoll, J.F. Effect of Heat Release and Swirl on the Recirculation within Swirl-Stabilized Flames. *Combust. Sci. Technol.* **1987**, *51*, 75–95. [CrossRef]
22. Wannassi, M.; Monnoyer, F. Numerical simulation of the flow through the blades of a swirl generator. *Appl. Math. Model.* **2014**, *40*, 1247–1259. [CrossRef]
23. Chong, C.T.; Hochgreb, S. Measurements of non-reacting and reacting flow fields of a liquid swirl flame burner. *Chin. J. Mech. Eng.* **2015**, *28*, 394–401. [CrossRef]
24. González-Espinosa, A.; Lozano, A.; García, J.A.; Barreras, F.; Lincheta, E. Design modification of the air diffuser in the burners of a fuel oil power plant. Part II: Interaction with the liquid spray. *Fuel* **2014**, *124*, 141–150. [CrossRef]
25. Arkhipov, V.A.; Matvienko, O.V.; Trofimov, V.F. Combustion of sprayed liquid fuel in a swirling flow. *Combust. Expl. Shock Waves* **2005**, *41*, 140–150. [CrossRef]
26. Bonefačić, I.; Wolf, I.; Blecich, P. Improvement of fuel oil spray combustion inside a 7 MW industrial furnace: A numerical study. *Appl. Therm. Eng.* **2017**, *110*, 795–804. [CrossRef]
27. Panchasara, H.V.; Simmons, B.M.; Agrawal, A.K.; Spear, S.K.; Daly, D.T. Combustion Performance of Biodiesel and Diesel-Vegetable Oil Blends in a Simulated Gas Turbine Burner. *J. Eng. Gas Turb. Power* **2009**, *131*, 031503. [CrossRef]
28. Yao, S.; Zhang, J.; Fang, T. Effect of viscosities on structure and instability of sprays from a swirl atomizer. *Exp. Therm. Fluid Sci.* **2012**, *39*, 158–166. [CrossRef]
29. Liu, M.; Duan, Y.; Zhang, T.; Xu, Y. Evaluation of unsteadiness in effervescent sprays by analysis of droplet arrival statistics—The influence of fluids properties and atomizer internal design. *Exp. Therm. Fluid Sci.* **2011**, *35*, 190–198. [CrossRef]
30. Lefebvre, A.H. Airblast atomization. *Prog. Energy Combust. Sci.* **1980**, *6*, 233–261. [CrossRef]

31. Kuchma, A.E.; Shchekin, A.K.; Lezova, A.A.; Martyukova, D.S. On the evolution of a multicomponent droplet during nonisothermal diffusion growth or evaporation. *Colloid J.* **2014**, *76*, 576–584. [CrossRef]
32. Yang, S.I.; Wu, M.S.; Hsu, T.C. Spray combustion characteristics of kerosene/bio-oil part I: Experimental study. *Energy* **2017**, *119*, 26–36. [CrossRef]
33. Wu, Z.; Bao, T.; Zhang, Q.; Deng, J.; Li, L. Simulation study on spray combustion mechanism of diesel-gasoline blend fuels. *Fuel* **2015**, *143*, 301–307. [CrossRef]
34. Johnson, M.R.; Littlejohn, D.; Nazeer, W.A.; Smith, K.O.; Cheng, R.K. A comparison of the flow fields and emissions of high-swirl injectors and low-swirl injectors for lean premixed gas turbines. *Proc. Combust. Inst.* **2005**, *30*, 2867–2874. [CrossRef]
35. Barreiros, A.; Carvalho, M.G.; Costa, M.; Lockwood, F.C. Prediction of the near burner region and measurements of NOx and particulate emissions in heavy fuel oil spray flames. *Combust. Flame* **1993**, *92*, 231–240. [CrossRef]
36. Ling, Z.; Zeng, X.; Ren, T.; Xu, H. Establishing a low-NOxand high-burnout performance in a large-scale, deep-air-staging laboratory furnace fired by a heavy-oil swirl burner. *Appl. Therm. Eng.* **2015**, *79*, 117–123. [CrossRef]
37. Jenny, P.; Roekaerts, D.; Beishuizen, N. Modeling of turbulent dilute spray combustion. *Prog. Energy Combust. Sci.* **2012**, *38*, 846–887. [CrossRef]
38. Chiu, H.H. Advances and challenges in droplet and spray combustion. I. Toward a unified theory of droplet aerothermochemistry. *Prog. Energy Combust. Sci.* **2000**, *26*, 381–416. [CrossRef]
39. Sirignano, W.A. Advances in droplet array combustion theory and modeling. *Prog. Energy Combust. Sci.* **2014**, *42*, 54–86. [CrossRef]
40. Basha, S.A.; Raja Gopal, K. In-cylinder fluid flow, turbulence and spray models—A review. *Renew. Sustain. Energy Rev.* **2009**, *13*, 1620–1627. [CrossRef]
41. ANSYS, Inc. *ANSYS® Workbench, Release 17.2 and 18.0*; Ansys Inc.: Canonsburg, PA, USA, 2017.
42. Teodorescu, P.; Stanescu, N.-D.; Andrea, N. Errors in numerical analysis. *Numer. Anal. Appl. Mech. Eng.* **2013**, 1–15. [CrossRef]
43. Vervisch, L. Using numerics to help the understanding of non-premixed turbulent flames. *Proc. Combust. Inst.* **2000**, *28*, 11–24. [CrossRef]
44. Shyy, W. *Computational Techniques for Complex Transport Phenomena*; Cambridge University Press: Cambridge, UK, 2005; ISBN 0-521-02360-2.
45. Pei, Y.; Hawkes, E.R.; Kook, S. Transported probability density function modelling of the vapour phase of an n-heptane jet at diesel engine conditions. *Proc. Combust. Inst.* **2013**, *34*, 3039–3047. [CrossRef]
46. Mohamed Ismail, H.; Ng, H.K.; Gan, S. Evaluation of non-premixed combustion and fuel spray models for in-cylinder diesel engine simulation. *Appl. Energy* **2012**, *90*, 271–279. [CrossRef]
47. Novella, R.; García, A.; Pastor, J.M.; Domenech, V. The role of detailed chemical kinetics on CFD diesel spray ignition and combustion modelling. *Math. Comput. Model.* **2011**, *54*, 1706–1719. [CrossRef]
48. Waibel, R.; Claxton, M. Burner design. In *The John Zink Combustion Handbook*; CRC Press LLC: Boca Raton, FL, USA, 2001; Chapter 11; pp. 351–370. ISBN 978-0-8493-2337-9.
49. Modest, M.F. The method of spherical harmonics (PN-approximation). In *Radiative Heat Transfer*; Academic Press: Cambridge MA, USA, 2003; Chapter 15.
50. A Total Look at Oil Burner Nozzles. Available online: http://www.delavaninc.com/pdf/total_look.pdf (accessed on 9 August 2015).
51. BurnerPartsWala Oil Burner Nozzles. Available online: http://www.burnerpartswala.com/index.php?option=com_content&view=article&id=105&Itemid=230 (accessed on 18 August 2015).
52. Hollow Cone Nozzles. Available online: http://www.lechler.de/Products/General-Industry/Hollow-cone-nozzles/-cba.N_AAABwYIAAAEvm4oh.E.A-en_US?FromContentSearch=1 (accessed on 23 January 2017).
53. Rimbert, N.; Castanet, G. Liquid atomization out of a full cone pressure swirl nozzle. In Proceedings of the 7th International Conference on Multiphase Flow ICMF 2010, Tampa, FL, USA, 30 May–4 June 2010; pp. 1–8.
54. Schmidt, D.P.; Nouar, I.; Senecal, P.K.; Rutland, C.J.; Martin, J.K.; Reitz, R.D.; Hoffman, J.A. Pressure-Swirl Atomization in the Near Field. *SAE Tech. Pap.* **1999**, *1999*. [CrossRef]
55. Senecal, P.K.; Schmidt, D.P.; Nouar, I.; Rutland, C.J.; Reitz, R.D.; Corradini, M.L. Modeling high speed viscous liquid sheet atomization. *Int. J. Multiph. Flow* **1999**, *25*, 1073–1097. [CrossRef]

56. Atomizer Models. Available online: http://jullio.pe.kr/fluent6.1/help/html/ug/node672.htm#sec-disp-spray-atom (accessed on 15 September 2016).
57. Glassman, I.; Yetter, R.A.; Glumac, N.G. Environmental combustion considerations. In *Combustion*; Academic Press: Cambridge MA, USA, 2015; Chapter 8; ISBN 978-0-12-407913-7.
58. ANSYS Inc. Prompt NOx Formation. In *ANSYS Fluent Theory Guide*; ANSYS Inc.: Canonsburg, PA, USA, 2016; Chapter 14.1.4.
59. ANSYS Inc. Pressure-velocity coupling. In *ANSYS Fluent Theory Guide*; ANSYS Inc.: Canonsburg, PA, USA, 2016; Chapter 21.
60. Incropera, F.P.; Dewitt, D.P.; Bergman, T.L.; Lavine, A.S. *Fundamentals of heat and mass transfer*, 6th ed.; John Wiley & Sons Inc.: Somerset, NJ, USA, 2007.
61. Gupta, A.K.; Lilley, D.G.; Syred, N. *Swirl Flows*; Energy and Engineering Science Series; Abacus Press: Tunbridge Wells, Kent, UK, 1984; ISBN 978-0-85626-175-6.
62. Bosch Motorsport Lambda Sensor LSU 4.9. Available online: http://www.bosch-motorsport.de/content/downloads/Products/18014401288629643.html# (accessed on 6 February 2017).
63. MKS MultiGas^{TM} 2030 FTIR Continuous Gas Analyzer. Available online: https://www.mksinst.com/product/product.aspx?ProductID=180 (accessed on 6 February 2017).
64. Twiss, S.B.; Teague, D.M.; Bozek, J.W.; Sink, M.V. Application of infrared spectroscopy to exhaust gas analysis. *J. Air Pollut. Control Assoc.* **2012**, *5*, 75–83. [CrossRef]
65. Lakshminarayanan, P.A.; Aswin, S. Estimation of particulate matter from smoke, oil consumption and fuel sulphur. *SAE Int.* **2016**, 1–11. [CrossRef]
66. Narasimhamurthy, V.D.; Andersson, H.I. Numerical simulation of the turbulent wake behind a normal flat plate. *Int. J. Heat Fluid Flow* **2009**, *30*, 1037–1043. [CrossRef]
67. Tian, X.; Ong, M.C.; Yang, J.; Myrhaug, D. Large-eddy simulation of the flow normal to a flat plate including corner effects at a high Reynolds number. *J. Fluids Struct.* **2014**, *49*, 149–169. [CrossRef]
68. ANSYS Inc. Reporting alphanumeric data. In *ANSYS Fluent Theory Guide*; ANSYS Inc.: Canonsburg, PA, USA, 2016; Chapter 23; p. 751.
69. Flagan, R.; Seinfeld, J.H. Combustion fundamentals. In *Fundamentals of Air Pollution Engineering*; Prentice-Hall, Inc.: Englewood Cliffs, NJ, USA, 1988; Chapter 2; ISBN 978-0-08-044106-1.
70. Missaghi, M.; Pourkashanian, M.; Williams, A.; Yap, L. The prediction of NO emissions from an industrial burner. In *American Flame Research Committee*; J. Willard Marriott Library, University of Utah: San Francisco, CA, USA, 1990.
71. Harmon, D.B. Drop sizes from low speed jets. *J. Frankl. Inst.* **1955**, *259*, 519–522. [CrossRef]
72. Tanasawa, Y.; Toyoda, S. *On the Atomization of Liquid Jet Issuing from a Cylindrical Nozzle*; Tohuku University: Tohuku, Japan, 1960.
73. Martınez-Martınez, S.; Sanchez-Cruz, F.A.; Riesco-Avila, J.M.; Gallegos-Munoz, A.; Aceves, S.M. Liquid penetration length in direct diesel fuel injection. *Appl. Therm. Eng.* **2008**, *28*, 1756–1762. [CrossRef]
74. Yu, S.; Reitz, R.D. Multi-dimensional modelling of diesel combustion: Review. In *Modelling Diesel Combustion*; Ling, F.F., Ed.; Springer Science+Business Media B.V.: Hosur-India, India, 2010; Chapter 15, ISBN 978-90-481-3884-5.
75. Jedelsky, J.; Jicha, M. Energy considerations in spraying process of a spill-return pressure-swirl atomizer. *Appl. Energy* **2014**, *132*, 485–495. [CrossRef]
76. Ribeiro, M.M.; Whitelaw, J.H. Coaxial jets with and without swirl. *J. Fluid Mech.* **1980**, *96*, 769. [CrossRef]